



Research Article

Multiphase Particle-in-Cell (MP-PIC) Simulation on Fluidization and Reaction Characteristics in an 80 kW Chemical Looping Gasification Unit

Cong Shen , Tuo Guo , Xiude Hu, Qingjie Guo* 

State Key Laboratory of High-Efficiency Utilization of Coal and Green Chemical Engineering, Ningxia University, Yinchuan, China

E-mail: qingjie_guo@vip.sina.com

Received: 6 April 2023; **Revised:** 28 April 2023; **Accepted:** 4 May 2023

Abstract: A numerical simulation study of the 80 kW Chemical Looping Gasification (CLG) pilot plant fuel reactor was conducted using the Computational Particle Fluid Dynamics (CPFD) method to investigate the influence of superficial gas velocity, coal particle size and static bed height on the gas-solid fluidization characteristics in the bed. The results showed that the suitable operating ranges were superficial gas velocity in 0.36~0.48 m/s, coal particle size in 0.3~0.4 mm, and static bed height in 0.6~0.8 m, and the CLG process released gas in the whole bed compared with the cold condition, which could effectively alleviate the uneven pressure gradient distribution. In addition, the working conditions with superficial gas velocity higher than 0.36 m/s, coal particle size higher than 0.35 mm and static bed height higher than 0.6 m are more favorable to the full contact between coal particles, oxygen carrier bed particles and gas phase, thus obtaining a higher carbon conversion rate.

Keywords: CLG, CPFD simulation, fluidized bed, gas-solid flow, coal gasification

1. Introduction

In the context of energy saving and emission reduction to curb the greenhouse effect, the development of emerging technologies for efficient conversion and utilization of traditional fossil fuels is one of the effective means to reduce direct CO₂ emissions.¹ In general, direct emissions of CO₂ can be reduced by developing new carbon make-up technologies.^{2,3} However, it is also possible to reduce system carbon emissions by improving the process approach to achieve internal separation of CO₂.⁴ Chemical Looping Gasification (CLG) is based on the principle of Chemical Looping Combustion (CLC), where oxygen carriers with metal oxides as the main component are used as a mass and heat transfer medium between the fuel reactor and the air reactor to produce clean gas in the fuel reactor as an oxygen source in the gasification process.⁵ When the oxygen carrier is recycled back to the fuel reactor, it will return the heat to maintain the gasification reaction, thus realizing the graded utilization of energy in the system,⁶ which is a new type of coal clean processing technology with great development potential.

For a long time, the vast majority of studies by researchers for CLG processes have been based on laboratory pilot-scale experiments focusing on the elemental migration characteristics and kinetic mechanisms of gasification reactions on thermogravimetric and pilot fluidized beds using specific oxygen carriers.⁷⁻⁹ However, it is difficult to conclude

favorably the process scale-up of CLG technology based on laboratory-scale devices limited by its industrial scale. At the same time, as a typical complex system of coupled gas-solid two-phase flow reaction, it is difficult to obtain the fluidization characteristics and reaction characteristics inside the device that can directly prove the continuous operation process by only relying on experiments. The use of computer software to simulate the process efficiency of the system¹⁰⁻¹² or the gas-solid fluidization characteristics in the reactor¹³⁻¹⁷ can greatly reduce the economic and time costs associated with trial-and-error experiments, and the validated mathematical model can also serve as a guide for the operation of the plant.

Flow simulation methods can be divided into Eulerian-Eulerian and Eulerian-Lagrangian methods according to the method of modeling the division of discrete and continuous phases in the system.¹⁸ Among them, the limitations of the Eulerian-Eulerian method in the partitioning of discrete and continuous phases make it difficult to obtain the motion of specific particles and thus be competent for the simulation of chemical looping processes.¹⁹ In contrast, the CFD-DEM and MP-PIC methods in the Euler-Lagrangian framework can trace the motion of specific particles and can efficiently solve the behavior of dense gas-solid flow reactions. However, the Computational Fluid Dynamics-Discrete Element Method (CFD-DEM) is difficult to efficiently complete the solution of flow reactions in large-scale reactors due to its limitations.²⁰ In contrast, the MP-PIC method treats homogeneous particles in a certain region as particle clusters and simplifies the collision behavior using a solid-state force model, which effectively reduces the computational workload of large-scale reactors and serves as an important tool for studying the flow reaction behavior of CLG reactors. Due to the early start of related research, the study of the CLC process has reached the pilot scale, for example, Kong et al.²¹ established a full-bed flow model for a pilot-scale CLC plant using the MP-PIC method, verified the accuracy of the model in both hydrodynamics and reaction kinetics by combining experimental phenomena, and determined the distribution characteristics of gas and solid phases during the cycle operation. The related study strongly demonstrates the accuracy of the MP-PIC method for modeling pilot-scale chemical looping processes. So far, most simulation studies for the CLG process have focused on the multiphase flow reaction behavior in laboratory-scale fluidized bed reactors. Guo et al.²² simulated the coal-coke pressurized CLG process on a laboratory-scale fluidized bed and analyzed it in the context of experimental phenomena. It was demonstrated that the pressurization achieved a positive regulation of the syngas component ratios by enhancing the coupling of the coal coke gasification reaction with the oxygen carrier reduction reaction. Li et al.^{23,24} conducted a simulation study of the problem of continuous feed CLG of biomass and petroleum coke based on iron-containing oxygen carriers in a bubbling fluidized bed fuel reactor, respectively. The results showed that the predicted syngas fraction outlet concentration in the reactor matches the trend in the literature.

In summary, the above study demonstrates that MP-PIC modeling simulations with coupled CLG reaction kinetic models can accurately reproduce the multiphase flow laws and reaction characteristics in pilot-scale CLG reactors, thus significantly reducing the economic costs used for pre-experiments. To determine the operating parameters of the actual plant and to obtain the regulation principles of CLG-related reactions on the fluidization characteristics, the cold and thermal models of the fuel reactor of the 80 kW CLG plant were established in this study with the apparent gas velocity, coal particle size and static bed height as variables, and the influence of CLG-related reactions on the fluidization characteristics was determined by comparing the differences between the cold and thermal fluidization characteristics. At the same time, the operating intervals of the corresponding parameters were determined and optimized according to the fluidization and reaction characteristics.

2. Simulation and experimental methods

2.1 Experimental methods and simulation conditions

The modeling object studied in this paper is the fuel reactor of the 0.24 t/d CLG pilot plant built by our group at the Ningdong pilot plant, and the device structure and model setting parameters of the fuel reactor are shown in Figure 1 and Table 1, respectively. The oxygen carrier enters the fuel reactor at the top return tube of the fuel reactor; the water vapor feed point is located at the annular air distribution duct at the bottom of the fuel reactor; the coal feed site is located at the wall in the middle position of the oxygen carrier bed in the dense phase section of the fuel reactor and is pushed into the fuel reactor at a constant mass flow rate through the screw feeder. The gas in the fuel reactor leaves the fuel reactor through the exhaust pipe at the top, and after stripping off the water vapor in the secondary condenser after

the exhaust pipe, it enters the gas component analysis equipment, a multi-component gas analyzer from MRU, Germany, for collection and analysis. The fuel reactor is designed as a bubble-bed reactor, which can extend the residence time of the fluidized gas in the fuel reactor while maintaining a relatively continuous outlet gas stream, thus allowing for a more complete reaction. Meanwhile, the reactor requires less water vapor than a turbulent bed and air bed reactors, which significantly reduces the energy consumption during the water vapor warming drive during operation. During operation, waste heat steam carries environmentally harmful substances such as tar and soot particles, so it needs to be condensed by a gas outlet condenser and stored in a condensate waste storage tank for uniform recovery.²⁵

Table 1. Operating parameters in experiment and simulation

Parameter		Value
Experiment	Simulation	
	$T_{FR}, ^\circ\text{C}$	950
	$M_{coal}, \text{g/s}$	0.5
	$\rho_{coal}, \text{kg/m}^3$	1,588.58
	$M_{OC}, \text{g/s}$	2
	$\rho_{OC}, \text{kg/m}^3$	3,540.91
	$M_{vapor}, \text{g/min}$	45
	Fluidized air composition	Water vapor (100%)
	P_{FR}, kPa	140
	Radius of OC, mm	0.106~0.125
	Radius of coal, mm	0.35~0.4
-	$v_{vapor}, \text{m/s}$	0.48
-	$T_{OC}, ^\circ\text{C}$	1,050
$T_{AR}, ^\circ\text{C}$	-	1,050
-	H_{OC}, m	0.65
Weight of OC Bed in FR, kg	-	7.5
Weight of OC Bed in AR, kg	-	4.5
Volume Flow Rate of Riser, L/min	-	50
-	Run Time, s	150

Table 2. Ultimate analysis and proximate analysis of Yangchangwan bituminous coal

Ultimate analysis (daf, wt%)					Proximate analysis (ad, wt%)				LHV
C	H	O	N	S	M	A	V	FC	MJ/kg
77.6	5.16	10.77	1.44	0.46	5.18	4.56	26.95	63.31	25.25

Table 3. The chemical component of ilmenite ore oxygen carrier

Compound	Fe ₂ O ₃	TiO ₂	SiO ₂	Al ₂ O ₃	CaO	MgO	Na ₂ O	MnO
wt%	43.34	18.89	18.77	7.49	4.85	3.28	2.28	1.10

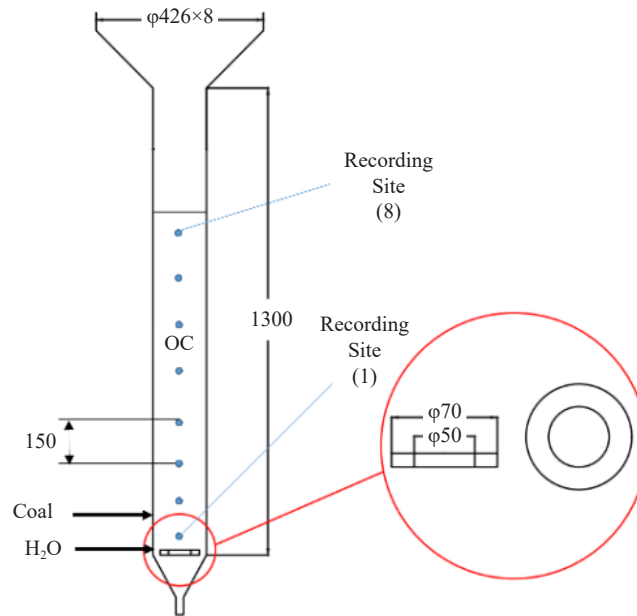


Figure 1. Schematic diagram of fuel reactor dimensions

In the simulation part, the fuel reactor was numerically simulated by the MP-PIC method using Barracuda Virtual software, and the time step was set to 1×10^{-3} s. In the simulation process, Yangchangwan bituminous coal from Ningxia was chosen as the fuel,²⁶ and its ultimate and proximate analyses are shown in Table 2. The fuel reactor bed material was selected from ilmenite oxygenates with better reactivity and greater mechanical strength, and the chemical composition of ilmenite oxygenates is shown in Table 3.^{27,28}

2.2 CPFD numerical model

The CPFD method employs a coupled Euler-Lagrange method to solve the three-dimensional motion of particles and fluid, with the fluid based on the Navier-Stokes equations and the particle phase calculated by the Multiphase Particle-in-Cell (MP-PIC) numerical method and coupled to the fluid phase by interphase traction.^{29,30}

2.2.1 Governing equations

Since the gas-solid two-phase flow studied in the following paper is approximately isothermal and the gas phase is considered incompressible, the energy equation does not need to be considered in the set of N-S equations. And for the gas-phase component, the control equation³¹ is:

$$\frac{\delta}{\delta t}(\alpha\rho)_g + \nabla(\alpha\rho u)_g = S_g \quad (1)$$

$$\frac{\delta}{\delta t}(\alpha \rho \mathbf{u})_{\text{g}} + \nabla(\alpha \rho \mathbf{u}^2)_{\text{g}} = -\nabla P + \rho_{\text{g}} \alpha_{\text{g}} \mathbf{g} + \nabla \cdot \alpha_{\text{g}} \tau_{\text{g}} - F \quad (2)$$

α_{g} is the volume fraction of the gas phase, ρ_{g} and \mathbf{u}_{g} are the density and velocity of the gas phase, respectively, S_{g} is the gas source term, P is the gas pressure, τ_{g} is the gas stress tensor, \mathbf{g} is the acceleration of gravity, and F is the interphase momentum exchange rate per unit volume. The momentum equation³² here neglects the viscous molecular diffusion and considers the viscous force F between the particle and the fluid as:

$$F = \int \int f m \left(D_{\text{p}}(\mathbf{u}_{\text{g}} - \mathbf{u}_{\text{p}}) - \frac{\nabla P}{\rho_{\text{p}}} \right) d m d v \quad (3)$$

D_{p} is the traction coefficient, v_{p} is the particle velocity, ρ_{p} is the particle density, and f is the probability distribution function, calculated from the following Liouville equation³³:

$$\frac{\delta f}{\delta t} + \nabla(f \mathbf{u}_{\text{p}}) + \nabla v_{\text{p}} \left(f \frac{d}{dt}(\mathbf{u}_{\text{p}}) \right) = 0 \quad (4)$$

$\frac{d}{dt}(\mathbf{u}_{\text{p}})$ is the particle acceleration, calculated from all the forces acting on the particle, and can be given by the MP-PIC method³⁴ as:

$$\frac{d}{dt}(\mathbf{u}_{\text{p}}) = D_{\text{p}}(\mathbf{u}_{\text{g}} - \mathbf{u}_{\text{p}}) - \frac{\nabla P}{\rho_{\text{p}}} - \frac{\nabla \cdot \tau_{\text{p}}}{\alpha_{\text{p}} \rho_{\text{p}}} + \mathbf{g} \quad (5)$$

τ_{p} is the inter-particle stress, α_{p} is the particle volume fraction. And the motion of the particles is given by the following equation:

$$\frac{d x_{\text{p}}}{dt} = \mathbf{u}_{\text{p}} \quad (6)$$

where x_{p} is the position vector of the tracked particles.

2.2.2 Drag equations

The Wen-Yu model, Ergun model, and Wen-Yu/Ergun model are all applicable to gas-solid homogeneous flow. Among them, the Wen-Yu model applies to gas-solid flows with particle volume fractions between 0.01 and 0.61, and the Ergun model applies to gas-solid flows with particle volume fractions between 0.47 and 0.7. The Wen-Yu/Ergun model is a linear transformation of the above two models, which enables the calculation of the traction force in systems with large concentration differences. In particular, the interphase traction function D_{p} in Eq. (3) is given by the following equation³⁵:

$$D_{\text{p}} = 4.5 \frac{\mu_{\text{g}}}{\rho_{\text{p}} r_{\text{p}}^2} f_{\text{b}} \quad (7)$$

where μ_{g} is the gas dynamic viscosity, r_{p} is the particle radius, and the coefficient f_{b} is determined by the following equation³⁶:

$$f_b = f_w \quad \alpha_p < 0.75\alpha_{cp} \quad (8)$$

$$f_b = f_w + \frac{\alpha_p - 0.75\alpha_{cp}}{0.1\alpha_{cp}}(f_e - f_w) \quad 0.75\alpha_{cp} \leq \alpha_p \leq 0.85\alpha_{cp} \quad (9)$$

$$f_b = f_e \quad \alpha_p > 0.85\alpha_{cp} \quad (10)$$

where α_{cp} is the volume fraction when the particles are tightly packed, and f_w and f_e are obtained from the Wen-Yu model and the Ergun model, respectively.

In the Wen-Yu model³⁷:

$$f_w = \alpha_g^{n_0} \quad Re < 0.5 \quad (11)$$

$$f_w = \alpha_g^{n_0} (c_0 + c_1 Re^{n_1}) \quad 0.5 \leq Re \leq 1000 \quad (12)$$

$$f_w = c_2 \frac{Re}{24} \alpha_g^{n_0} \quad Re > 1000 \quad (13)$$

Where, n_0, n_1, c_0, c_1, c_2 are constants, and the recommended values are $n_0 = -2.65, n_1 = 0.687, c_0 = 1.0, c_1 = 0.15, c_2 = 0.44$. Re is calculated by Eq. (15).

In the Ergun model:

$$f_e = \left\{ \frac{1}{18} c_3 Re + c_4 \frac{\alpha_p}{\alpha_g} \right\} \quad (14)$$

Where c_3, c_4 are constants, the recommended value $c_3 = 2.0, c_4 = 180$.

$$Re = \frac{2\rho_g r_p |\mathbf{u}_g - \mathbf{u}_p|}{\mu_g} \quad (15)$$

2.2.3 Solid stress model

Inter-particle collisions using the particle law phase-direction stress model:

$$\tau_p = \frac{P_s \alpha_p^\gamma}{\max[(\alpha_{cp} - \alpha_p), \varepsilon(1 - \alpha_p)]} \quad (16)$$

where P_s is a positive constant with a default value of $1.2 \leq \gamma \leq 5$ is the model's parameter, and ε is a small quantity of order 10^{-7} constructed to eliminate singularities in the model.

2.3 Reaction kinetic model

2.3.1 Coal pyrolysis reaction

Because of the high-temperature condition in the environment, coal undergoes a rapid pyrolysis process when enters the reactor. Based on the industrial and elemental analysis of the coal used in this experiment, the pyrolysis

reaction of coal is expressed as follows, according to the model given by Wang et al.³⁸:



This kinetic equation for pyrolysis can be expressed as Eq. (18):

$$R_{\text{pyrolyze}} = (Y_a k_a + Y_b k_b) C_{\text{coal}} \quad (18)$$

where C_{coal} denotes the concentration of coal and k_b is the pyrolysis reaction rate constant, obtained from Table 4 through the Arrhenius equation:

Table 4. Kinetic parameters of coal pyrolysis

Parameter type	E, kJ/mol	A, s ⁻¹	Y
a	104.6	2×10 ⁵	0.3
b	167.4	1.3×10 ⁷	1.0

2.3.2 Coal-coke gasification reaction

After pyrolysis, the resulting coal coke undergoes a gasification reaction in contact with the gasification agent, which is H₂O. The main reactions that occur in this process are shown in (19) and (20).³⁹



Table 5. Kinetic parameters of coal gasification

Gasification	E ₁	A ₁	E ₂	A ₂	E ₃	A ₁
Agent	kJ/mol	m ³ /(mol·s)	kJ/mol	m ³ /(mol·s)	kJ/mol	m ³ /(mol·s)
H ₂ O	1.27 × 10 ²	9.62	5.86 × 10 ⁻²⁸	6.02 × 10 ⁻⁴	0.74 × 10 ²	11.55
CO ₂	2.8 × 10 ²	1.02 × 10 ⁸	1.31 × 10 ²	6.43 × 10 ³	-0.72 × 10 ²	1.17 × 10 ⁻⁴

The decisive rate step of coal coke gasification reaction rate after pyrolysis is kinetically controlled and the rate of coal-coke gasification (R_g , mol·s⁻¹·m⁻³) was calculated using the Langmuir-Hinshelwood equation Eq. (21) form.⁴⁰

$$R_g = \frac{k_1 c_{\text{rea}}}{1 + k_2 c_{\text{rea}} + k_3 c_{\text{pro}}} \cdot \frac{0.85 m_c}{12\pi \left(\frac{d_{\text{rea}}}{2}\right)^2 h} \quad (21)$$

where m_c is the mass of coal coke after pyrolysis, g; d_{rea} is the reactor inner diameter, m; h is the reactor height, m; c_{rea}

is the concentration of gasification agent, $\text{mol}\cdot\text{m}^{-3}$; c_{pro} is the concentration of gasification products, $\text{mol}\cdot\text{m}^{-3}$; k is the reaction rate constant, $\text{m}^3\cdot\text{mol}^{-1}\cdot\text{s}^{-1}$, obtained from Table 5 via the Arrhenius equation.

2.3.3 Water gas shift reaction

In the process of pyrolysis and gasification, the gas phase product CO can undergo a water gas shift reaction with H_2O to produce CO_2 and H_2 , thus changing the ratio of components in the gas phase product. In the industrial production of coal gasification, this method is often used to adjust the hydrogen/carbon ratio in syngas, as shown in (22) and Table 6.⁴¹

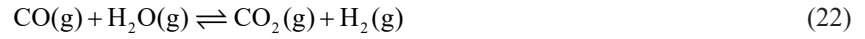
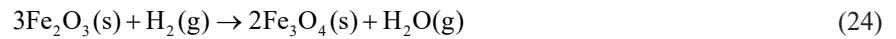
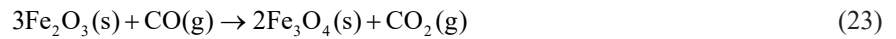


Table 6. Reactions kinetics of the Water-Gas Shift Reaction

Reaction	Reaction rate
R4- positive reaction	$R_{4,p} = 2.78 \cdot 10^3 [\text{CO}][\text{H}_2\text{O}] \exp\left(-1.26 \cdot \frac{10^7}{RT}\right)$
R4- counter reaction	$R_{4,c} = 9.59 \cdot 10^4 [\text{CO}_2][\text{H}_2] \exp\left(-4.66 \cdot \frac{10^7}{RT}\right)$

2.3.4 Oxygen carrier reduction reaction

According to the content of the ilmenite oxygen carrier components described in the previous section, the effective component of the ilmenite oxygen carrier is Fe_2O_3 . In the fuel reactor, this effective component is reduced to three reduced states, Fe_3O_4 , FeO , and Fe , depending on the depth of lattice oxygen release. In the previous experiments, no single Fe was observed in the reduced oxygen carrier, while Fe_3O_4 can be regarded as a mixture of Fe_2O_3 and FeO mixture, so the main reflection of the oxygen carrier occurring at this stage can be represented by the reactions (23) and (24).



The reaction is performed using the Shrinking Core Model (SCM), and the model equation is shown in Eq. (25).⁴² Where x_{OC} is the conversion rate of the oxygen carrier reduction reaction; τ is the time required for the complete reduction conversion of the oxygen carrier, s, obtained from Eq. (26), where b is the stoichiometric number; ρ_m is the molar density of the oxygen carrier, $\text{mol}\cdot\text{m}^{-3}$; L is the characteristic length of Fe_2O_3 grains, 2.6×10^{-7} m; c_g^n is the number of reductions including the reaction level gas concentration, $\text{moln}\cdot\text{m}^{-3}$.

$$\frac{t}{\tau} = 1 - (1 - x_{\text{OC}})^{1/3} \quad (25)$$

$$\tau = \frac{\rho_m L}{bkc_g^n} \quad (26)$$

Eq. (27) is the formula for the rate of oxygen carrier reduction reaction (R_r , $\text{mol}\cdot\text{s}^{-1}\cdot\text{m}^{-3}$), where m_{OC} is the amount of oxygen carrier added, g; other kinetic parameters are shown in Table 7.⁴³

$$R_r = \frac{bAc_g^n \exp(-E/RT)}{\rho_m L} \cdot \frac{0.4m_{\text{OC}}}{12\pi\left(\frac{d_{\text{rea}}}{2}\right)^2 h} \quad (27)$$

Table 7. Reduction kinetic parameters of OC

Equation	b	A	E	n
		$\text{mol}^{1-n}\text{m}^{3n-2}\text{s}^{-1}$	$\text{kJ}\cdot\text{mol}^{-1}$	
23	3.0	6.2×10^{-4}	20	1.0
24	3.0	2.3×10^{-3}	24	0.8

b: Stoichiometric factor; E: Activation energy; A: Pre-exponential factor

3. Model validation

3.1 Cold condition

To determine the accuracy of the model for the fluidization characteristics, the differential pressure values obtained from the simulation and the experiment were taken and compared as shown in Table 8. As can be seen from the table, the experiments agree with the simulations and are within the acceptable error range of the data.

Table 8. Comparison of experiment and simulation (Fluidization characteristic)

Height, m	Simulation gauge pressure (kPa)	Experiment gauge pressure (kPa)	Deviation (%)
0	123.4	123.5	0.6
0.6	107.8	105.5	2.17
1.05	101.5	101.2	0.78

3.2 Thermal condition

To determine the accuracy of the chemical reaction model, the volume fractions of the fuel reactor outlet gas obtained from experiments and simulations in the whole region were used as a reference, and the comparison results are shown in Table 9. It can be seen from the table that the proportions of the fuel reactor outlet gas components in the experimental and simulated groups are in agreement. the deviation of the CO volume fraction is about 1.56%, the CO₂ volume fraction is about 7.96%, and the H₂ volume fraction is about 1.70%, which indicates that the simulation results are plausible.

To determine the accuracy of the heat flow model, the gauge pressures obtained from the experiments and simulations are shown in Table 10 below. As can be seen from the table, the simulated data of pressure drop at the recording points of the experimental setup are consistent and are within the acceptable data error.

Table 9. Comparison of experiment and simulation (Reaction characteristic)

Component	Simulation mole fraction (%)	Experiment mole fraction (%)	Deviation (%)
CO	9.39	9.24	1.56
CO ₂	17.67	19.07	7.96
H ₂	72.92	71.67	1.70

Table 10. Comparison of experiment and simulation (Fluidization characteristic)

Height, m	Simulation gauge pressure (kPa)	Experiment gauge pressure (kPa)	Deviation (%)
0	120.1	121.5	1.16
0.6	106.7	106.5	0.2
1.05	101.7	101.2	0.5

4. Cold-state simulation

4.1 Superficial gas velocity

Superficial gas velocity is the main influencing factor of the gas-solid fluidization condition. With the increase of superficial gas velocity, the complexity of gas-solid motion will increase. According to the design parameters of this device, the values of superficial gas velocity are set to 0.12 m/s, 0.24 m/s, 0.36 m/s, 0.48 m/s, and 0.6 m/s in the cold-state simulation to determine the superficial gas velocity operating range, the height of oxygen carrier static bed is 0.6 m, the circulation flux of oxygen carrier is 1.2 kg/h, the inlet pressure of fluidized air is 140,000 Pa, the outlet pressure is 101,325 Pa, and the fluidized air inlet component is 100% water vapor.

The gas-solid flow performance of the bed in the fuel reactor at different superficial gas velocities is shown in Figure 2. Figure 2(a) shows the variation of the gauge pressure between the points in the bed showing a trend of first increasing and then decreasing with the increase of the superficial gas velocity. When the superficial gas velocity is 0.12 m/s, the gauge pressure in the whole bed is the lowest value. When the superficial gas velocity continued to rise to 0.36 m/s, the gauge pressure was the highest value in the whole bed range, and then the gauge pressure value gradually decreased with the increase of the superficial gas velocity. Figure 2(b) shows that when the superficial gas velocity of the fluidized gas inlet is 0.12 m/s, individual bubbles in the bed cannot overcome the particle accumulation resistance leading to the difficulty of merging adjacent bubbles during the ascending process, thus the distribution of bubbles in the whole bed shows the trend of dispersed distribution with small volume and large number. Thereafter, as the superficial gas velocity continued to increase to 0.36 m/s, the increased gas dosage gave the kinetic energy to the bubbles at the bottom of the bed to overcome the bed particle pressure resistance, which enabled the small bubbles to expand rapidly after formation and merge to form larger bubbles. When the superficial gas velocity range is in 0.36~0.48 m/s, the bubbles, and the surrounding particle bed accumulation resistance reach a dynamic equilibrium balance in the whole bed range, so that the trajectory of bubbles returns to the reactor midline, which also ensures the residence time of fluidized gas in the bed. When the superficial gas velocity continues to rise to 0.6 m/s, the excess gas volume breaks the force equilibrium between the gas and solid phases, causing the bubbles to grow out of control in terms of volume expansion rate and rise rate. This bed performance will cause severe trench flow and hinder the mass and heat transfer between the gas and solid phases in the bed. Therefore, the selected interval of superficial gas velocity should be 0.36~0.48 m/s.

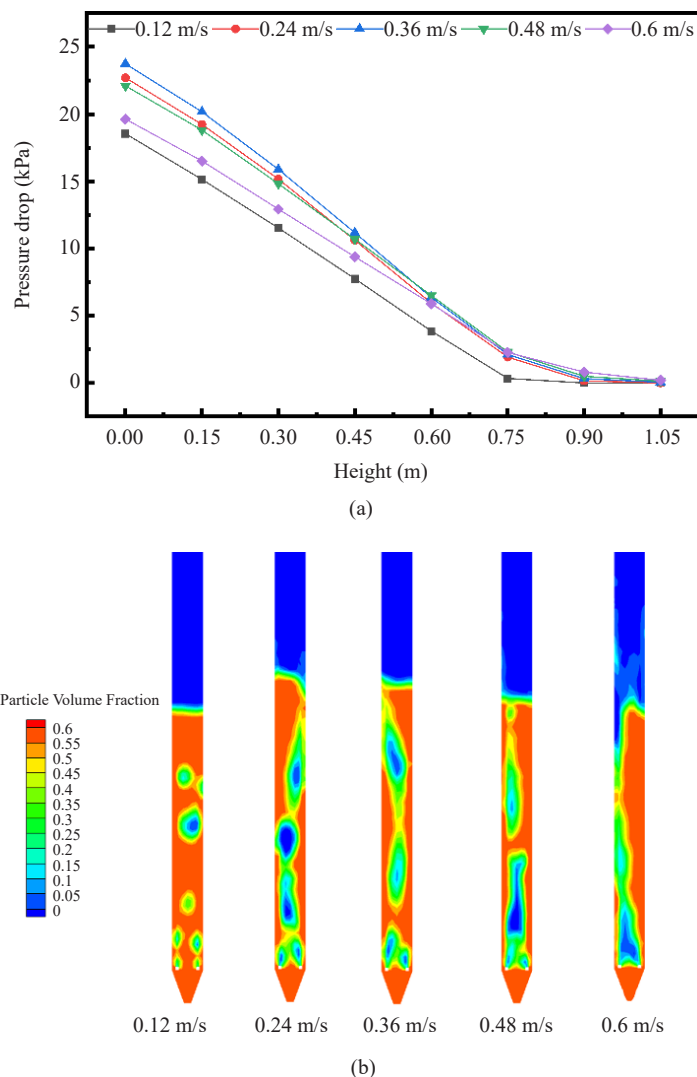


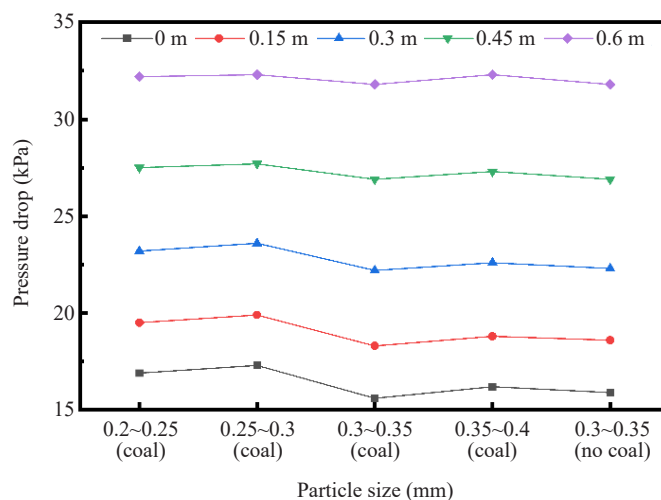
Figure 2. Effects of fluidized air inlet velocity on gas-solid fluidization characteristic (a). gauge pressure; (b). particle distribution

4.2 Coal particle size

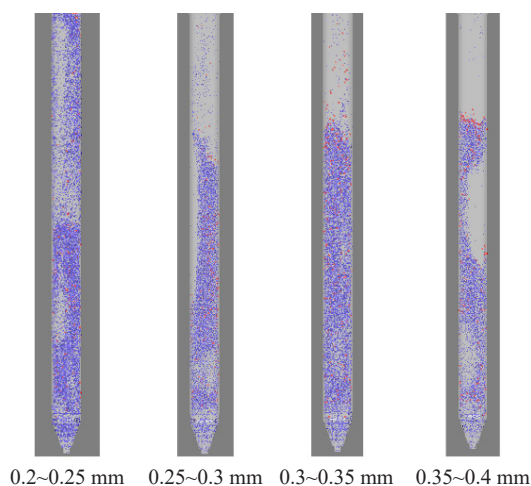
Although the amount of coal is relatively few in the total amount of full bed particles, different coal particle sizes still cause differences in their distribution characteristics in the fuel reactor.^{44,45} Therefore, to determine the coal particle size, the coal particle size was divided into four particle radii of 0.2 to 0.25 mm, 0.25 to 0.3 mm, 0.3 to 0.35 mm, and 0.35 to 0.4 mm for cold-state simulation according to the handling capacity of the mill equipped with the experimental setup. Other boundary conditions setting values are consistent with the 1.2 m/s simulation group in 3.2.

The effect of coal particle size on the gas-solid fluidization characteristics of the fuel reactor bed is illustrated in Figure 3. When the coal particle size is less than 0.3 mm, the effect of airflow traction on coal particles is more pronounced, and this uneven traction effect causes the bed pressure drop to increase over the full bed compared to the no-coal addition condition. At the same time, the air bubbles in the middle and upper regions of the bed are more likely to rupture near the middle of the bed and cause serious precipitation, which will blow a large number of particles into the region above the bed and form a large volume of dilute phase cavity in the region near the top of the bed, which will seriously hinder the mass and heat transfer reaction process of each component in this region. When the coal particles increase to 0.3 mm or more, the effect of airflow traction on the particles of the two components in the bed is gradually balanced, so that the bed motion trend returns to the situation without coal addition and stabilizes the fluidization state

in the whole bed. However, when the coal particle size is higher than 0.35 mm, although the coal will not cause uneven force on the particles after rising to the top of the bed, it will form an accumulation area at the top of the bed which is difficult to be driven by the expanding bed, and this phenomenon may hinder the mass and heat transfer process thereafter. Therefore, the operating range of coal particle size should be 0.3~0.35 mm.



(a)



(b)

Figure 3. Effects of coal particle size on gas-solid fluidization characteristic (cold state) (a). Pressure drop; (b). Particle specie (50 s)

4.3 Static bed height

The effect of the static bed height on the axial time-averaged pressure gradient in the fuel reactor bed is illustrated in Figure 4. The figure shows that when the static bed height is below 0.6 m, the axial pressure gradient is more uniformly distributed over the whole bed. When the static bed height increases, the rising resistance to airflow impedes the rising tendency of bubbles in the middle and lower regions of the bed, which leads to a significantly higher tendency of merging between bubbles. The excessive merging behavior of the bubbles at the bottom of the bed breaks the force balance between the gas-solid phases, causing the bubbles to pass rapidly through the bed space in the middle and upper regions, which in turn causes the pressure gradient in this region to show a rapid pressure drop. As can be seen in the figure, when the static bed height is 0.6 m, the shape, size, and velocity of the bubbles can still be well controlled when

they pass through the bed, although the trend of uncontrolled growth has already appeared. After that, the increase of the static bed height will further aggravate the tendency of merging the bubbles at the bottom of the bed, and even form a serious tumbling phenomenon in the middle and upper regions of the bed. This will seriously affect the fluidization stability of the upper and middle beds and is not conducive to the gas-solid heat transfer behavior inside the upper and middle parts of the bed. Therefore, the static bed height should not be too high, but should also avoid the low height resulting in a lower residence time of the gas in the bed, which should be 0.6 m.

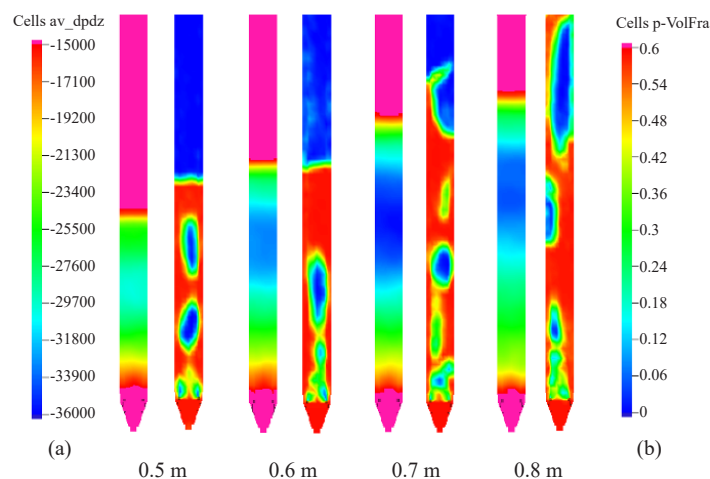


Figure 4. Effect of OC height on gas-solid fluidization characteristic (a). av-dp/dz; (b). Particle volume fraction

5. Thermal-state simulation

5.1 Differences in macroscopic fluidization characteristics between cold and thermal states

In Figure 5, the differences in gas-solid flow behavior exhibited by the cold and thermal simulations under the same boundary conditions are compared, and it can be seen that the introduction of chemical reactions significantly changes the gas-solid flow state in the fuel reactor. Figure 5(a) shows that the presence of CLG-related reactions significantly increases the gas flow through the fuel reactor, thus reducing the gauge pressure values at each pressure record point. This phenomenon is consistent with the simulation group with a superficial gas velocity above 0.9 m/s.⁴⁶ Figure 5(b) shows that the distribution of coal particles inside the fuel reactor is significantly reduced in the thermal condition compared to the cold condition. This is because as the gasification reaction proceeds, the consumption of fixed carbon and volatile fraction in coal particles causes a significant decrease in particle mass, resulting in a significant entrainment effect of the updraft. Meanwhile, a large amount of gas is generated from the surface of the coal due to the gasification, thus creating an additional trapping effect on it, which aggravates its tendency to move in the direction of airflow motion. In Figure 5(c), the time-averaged axial pressure gradient in the cold state is compared with that in the thermal state. It shows that the released gas components not only form an additional trapping force on the coal during the gasification reaction proceeding, but the same effect also acts on the oxygen carrier bed particles around the coal particles at the same time, which weakens the obstruction of the updraft by the particle buildup and makes the pressure gradient in the bed more uniformly distributed.

In the simulation, real-time mass-volume flow rate information of the gas components can be output by setting the gas output surface at the fuel reactor outlet location, while the post-processing software can directly obtain the spatial distribution of each component gas. To investigate the causes of the differences in the gas-solid fluidization characteristics caused in the thermal and cold simulations of CLG, the mass fraction distribution of the different gas components in the fuel reactor in the thermal simulation is compared in Figure 6. Although CO and H₂ components are the target products of the CLG process, both components are consumed simultaneously due to their reaction with

oxygen carriers in the bed. Therefore, the mass fractions of CO and H₂ in the bed are relatively low and more distributed in the area above the bed height. And CO₂, as the reaction product between CO and oxygen carrier, is widely distributed in the upper space in the fuel reactor. In summary, it can be seen that the gaseous products released by the chemical reaction in the full bed range are the direct cause of the difference in gas-solid fluidization characteristics of the CLG process. Among the syngas components generated in the reactor, CO₂ has the most uniform distribution in the bed and is the main source of additional drag force of the bed particles.

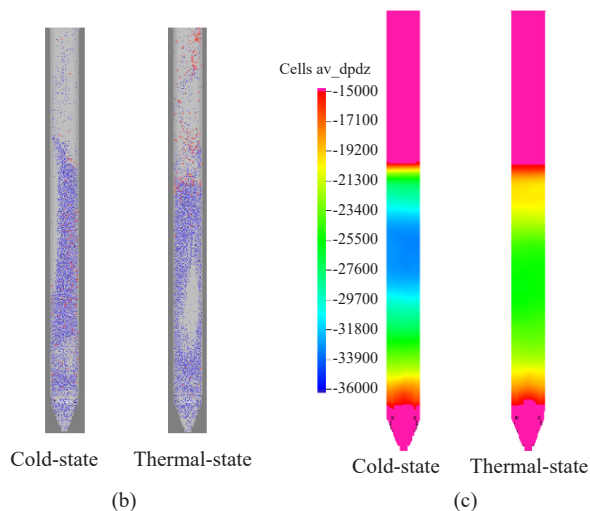
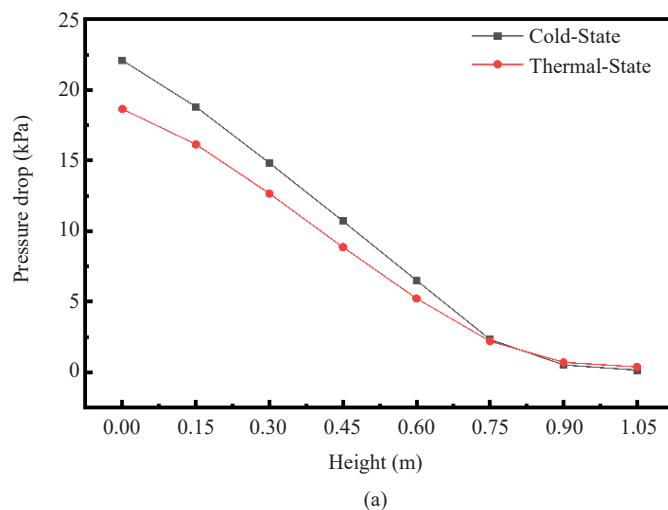


Figure 5. Comparison of cold and thermal state gas-solid fluidization characteristics. (a). gauge pressure; (b). Particle type distribution (red - coal and derived particles; blue - oxygen carrier particles); (c). time-averaged axial pressure gradient

5.2 Thermal fluidization and reaction characteristics

5.2.1 Superficial gas velocity

For the kW-scale CLG pilot plant, the superficial gas velocity of the fuel reactor is directly related to the water vapor dosage; the higher the superficial gas velocity, the higher the water vapor dosage. It has been shown that maintaining a high water vapor dosage has a facilitating effect on maintaining the coal gasification process. In a previous simulation of the CLG process based on Aspen Plus software,^{47,48} the effect of water vapor dosage on the syngas fraction at the exit of the CLG process was investigated. However, in addition to the direct participation in the chemical reaction

process, water vapor affects the fluidization characteristics of the gas-solid flow system as a component of the fluidized gas, and a larger water vapor dosage implies a larger superficial gas velocity, which is not favorable for the gas residence in the bed. At the same time, since water vapor has a large specific heat capacity, an excessive water vapor flow rate will carry more sensible heat out of the system, resulting in higher heat loss of the system. Therefore, several simulation groups based on 1.2 m/s fluidized gas velocity conditions were carried out to vary the water vapor dosage by changing the partial pressure of water vapor in the inlet fluidized gas.

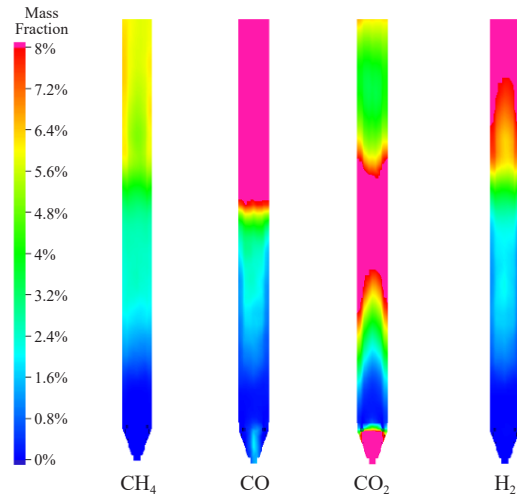


Figure 6. Time-averaged distribution characteristics of syngas

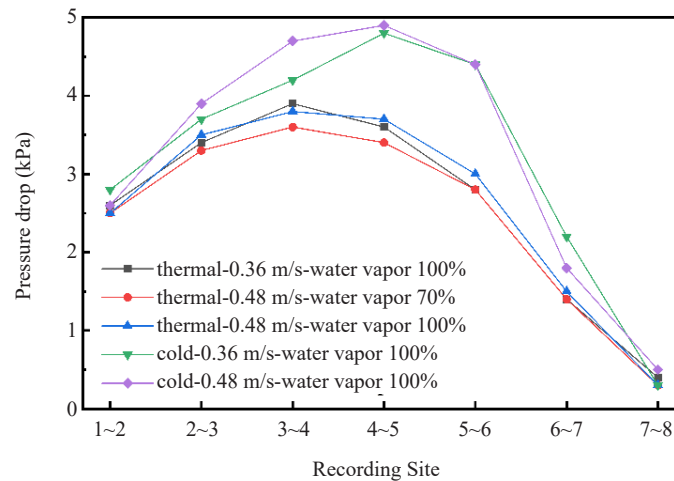


Figure 7. Effect of water vapor mass rate on pressure drop

The effects of different water vapor parameter conditions on the gas-solid fluidization characteristics and reaction characteristics of the system are shown in Figure 7 and Table 10, respectively. By comparing the pressure drop data and reaction data of different fluidized gas superficial gas velocity thermal state simulation groups under 100% water vapor feed, it can be found that the bed pressure drop distribution is more uniform in groups 2 and 3 compared with group 1, and there is no area with larger pressure drop increment. This is implied that more total bottom updraft can strengthen its ability to overcome the resistance of the particle bed to move upward. As can be seen in Figure 7, the pressure drop between each recording point in the thermal state simulation decreases more significantly than in the cold state

group, which indicates that the distribution of gas released from the gasification reaction over the full bed increases the effect of the trapping force on the bed particles, thus reducing the resistance of the gas during the ascent process. This phenomenon has a positive effect on maintaining bed stability during operation.

The exported syngas components and quality for different water vapor dosages are presented in Table 11. The comparison of the data in the table shows that for the simulated group with the same amount of water vapor, increasing the superficial gas velocity by adding other inert gases can effectively enhance the CLG process and thus significantly increase the carbon conversion rate and syngas yield. However, this improvement in fuel utilization efficiency is limited and it is not possible to increase the carbon conversion rate and syngas yield to the 100% water vapor content group at the same superficial gas velocity.

Table 11. Effect of flow velocity on gasification performance

No.	Vapor pressure	v_{vapor}	Vapor/Coal (mass ratio)	V_{H_2}	η_{cg}	X_{carbon}
	%	m/s	-	NL/g	%	%
1	100	0.36	1.17	0.5077	58.5	52.7
2	70	0.48	1.17	0.5152	61.1	60.8
3	100	0.48	1.56	0.5794	68.0	67.8

5.2.2 Coal particle size

A plot of the fuel reactor pressure drop trend for different feed particle sizes of coal in the thermal simulation is shown in Figure 8(a). It can be seen from the figure that the chemical reaction significantly increases the full-bed pressure drop and eliminates the trend of decreasing bed pressure drop with increasing coal particle size. The spatial trend of each particle in the fuel reactor at different particle sizes is shown in Figure 8(b). It can be seen from the figure that although the introduction of chemical reactions significantly reduces the number of coal particles distributed in the lower and middle regions of the bed, the larger particle sizes can maintain a higher number of coal particles distributed in the bed relative to the smaller particle sizes. This results in more adequate contact between coal particles and the oxygen carrier bed and, coal and fluidized gas.

Table 12 shows the variation of cold gas efficiency and the yield of different gas components with the interval of coal particle size. From the table, it can be seen that the change in coal particle size has less effect on each group of data, but still shows a trend that the cold gas efficiency decreases first and then increases. The cold gas efficiency decreases from 76.6% at 0.2-0.25 mm to 75.8% between 0.25-0.3 mm and then increases to 77.1% at 0.4 mm. This implies that multiple variables significantly affect the CLG reaction process as the coal particle size increases and enhances the chemical reaction process in the fuel reactor in different ways at different particle sizes. When the coal particle size is less than 0.3 mm, the promotion of coal gasification by small particle size is less than the inhibition of the gasification process by short residence time as the coal particle size increases, resulting in a slight decrease in the yield of the syngas fraction. When the particle size was larger than 0.3 mm, the residence time of coal particles in the bed was prolonged significantly, and more CO reacted with oxygen carriers in the bed, thus significantly increasing the yield of CO₂, so that the increment of CO₂ then reached 82.4% of the total increment of carbonaceous gas. This implies that increasing the residence time of coal particles in the bed increases the carbon conversion rate mainly by increasing the CO₂ yield.

It can be seen that the introduction of chemical reactions can have a large impact on the distribution characteristics of coal particles in the bed. Coal particles with a smaller radius and longer residence time have faster reaction rates and thus higher cold gas efficiency and fuel utilization efficiency. However, smaller coal particle size will shorten the residence time of coal particles in the bed space and form a buildup area at the top of the bed within a short time of entering the reactor, which seriously hinders the mass and heat transfer process and significantly reduces the fuel utilization efficiency of the system. Higher coal particle size can maintain the carbon conversion rate of the system at a

high level by maintaining the residence time of coal particles in the middle of the bed, but the incremental carbonaceous gas is dominated by CO₂ due to the presence of the effective fraction of oxygen carriers in the bed particles.

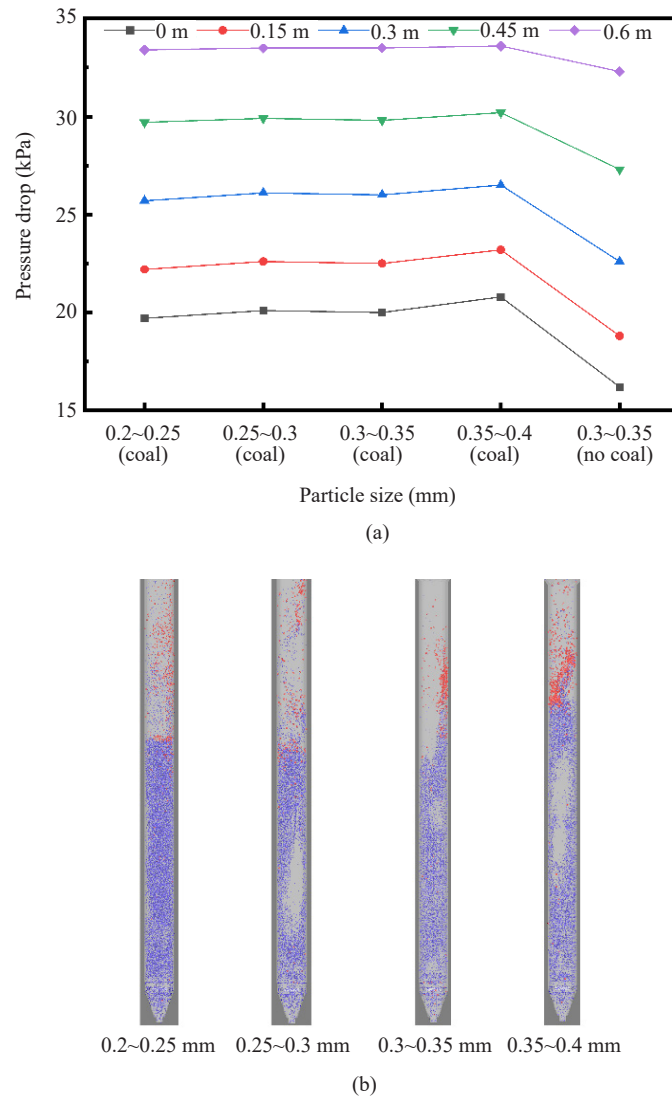


Figure 8. Effects of coal particle radius distribution on gas-solid fluidization characteristic. (thermal state) (a). Pressure drop; (b). Particle specie (150 s)

Table 12. Effects of coal particle size on syngas quality paraments

R_{coal}	η_{eg}	X_{carbon}	V_{CO_2}	V_{CO}	V_{H_2}
mm	(%)	(%)	NL/g	NL/g	NL/g
0.2~0.25	76.6	65.8	0.457	0.290	1.168
0.25~0.3	75.8	67.0	0.474	0.287	1.156
0.3~0.35	76.2	67.8	0.477	0.293	1.158
0.35~0.4	77.1	70.1	0.498	0.298	1.171

5.2.3 Static bed height

Figure 9 shows the effect of chemical reactions on the axial pressure gradient in the fuel reactor for different static bed heights of oxygen carriers. The conclusions in 4.2 demonstrate that the release of gas in the full-bed range in the thermal condition reduces the obstructive effect of the bed buildup on the gas flow, which is more pronounced in the low static bed height. However, the low static bed height results in a lower mass of particle buildup, which prevents it from forming an effective obstruction to the gas flow and thus breaks the transmission equilibrium between the gas and solid phases, resulting in a non-uniform pressure gradient distribution in the low-bed group. This further destabilizes the fluidization of the bubbling bed and reduces the residence time of the water vapor. And precisely because the presence of the chemical reaction averages the pressure gradient across the bed, it alleviates the uneven pressure gradient distribution that occurs in the cold state high static bed group. This facilitates the control of the volume growth and rise rate during bubble movement, thus maintaining a uniform velocity and size of the bubbles through the bed, which has a positive impact on maintaining bed stability and sufficient residence time of the gas in the bed.

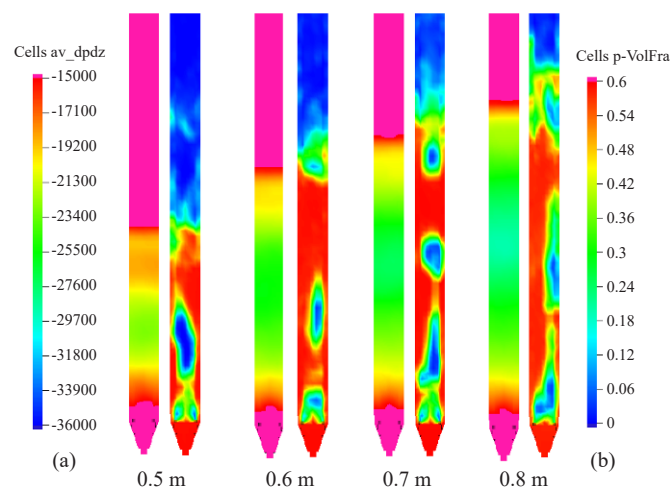


Figure 9. Effects of the height of OC bed on time-averaged pressure gradient (a). av-dp/dz; (b). Particle volume fraction

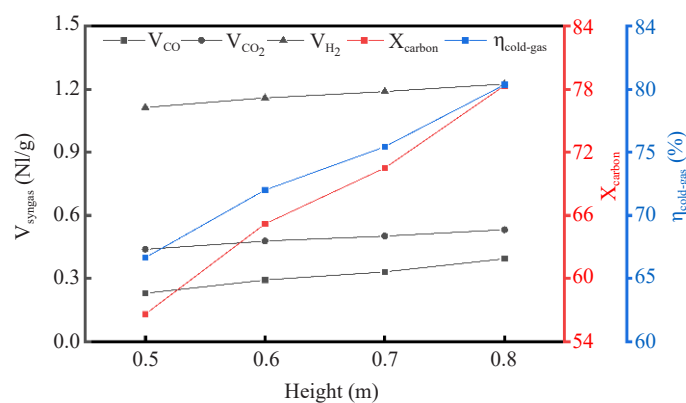


Figure 10. Effect of static bed height on gasification performance

The effects of different static bed heights on the CLG performance are presented in Figure 10. The figure shows that the yield of syngas components such as CO, CO₂, and H₂ increases uniformly with the increase of static bed height,

with a larger increase in the stage from 0.5 m to 0.6 m. The increase of the molar fraction of CO, CO₂, and H₂ in the exit gas is 27.3%, 8.8%, and 4.0%. Meanwhile, the carbon conversion rate and cold gas efficiency both experienced the largest increase in the whole process when the static bed height increased from 0.5 m to 0.6 m. The production of both CO and CO₂ tended to increase with the increase of the static bed height. However, the increase of CO production is larger than that of CO₂ throughout the process, which indicates that the higher static bed height conditions can promote the fuel conversion efficiency and also the trend of coke to CO conversion, thus increasing the effective conversion of fixed carbon.

In summary, the gas released by the CLG process creates an additional traction effect on the particle bed, thus reducing the drag effect on the rising gas phase and creating an effective modulation of the pressure gradient distribution over the full bed range. This modulating effect is more evident in high static bed systems. The gas released from the chemical reaction increases the gas phase flux through the fuel reactor bed, balancing the particle resistance caused by the increase in static bed height, so that the gas phase no longer appears due to bubble aggregation during the ascent. Thus, the high static bed group obtains a high syngas yield and cold gas efficiency. Therefore, after the optimization of the thermal flow reaction simulation, it was determined that the applicable static bed height of the unit should be higher than 0.6 m.

6. Conclusions

In this work, a CPFD flow reaction model was developed based on the fuel reactor system of the kW-scale CLG pilot plant based on the bituminous coal of Yangchangwan, Ningxia, and the accuracy of the model was verified by combining partial thermal-state continuous feeding experiments. And then the operating range of three variables: superficial gas velocity, coal particle size, and static bed height, were determined by a combination of cold and thermal simulations, and the differences of gas-solid fluidization characteristics presented by the above variables in the cold and thermal simulations were discussed in depth. The main conclusions are as follows.

(1) Superficial gas velocity can significantly influence the fluidization characteristics of the reactor bed by changing the fluidized gas drive potential and is the most critical factor affecting the fluidization characteristics in this stage. Maintaining a high fluidized gas velocity can enhance the CLG process. However, too high fluidized gas velocity will cause frequent channel flow in the bed, which will adversely affect the stable operation of the plant.

(2) Increasing the coal particle size will finitely reduce the resistance of bed particles to the gas flow. The CLG-related reaction will increase the full-bed gas flow, which will offset the performance of coal particle size change on the bed resistance and significantly reduce the residence time of coal particles in the bed. However, when the coal particle size is kept at 0.3~0.4 mm it is still able to maintain relatively long in-bed residence time and obtain higher fuel utilization efficiency.

(3) The gas dominated by the CO₂ component forms an additional traction effect on the stacked oxygen-carrying particles, which significantly reduces the drag effect on the gas during the ascent and equalizes the pressure gradient distribution across the bed under high static bed conditions. This effectively avoids the generation of the phenomenon of tumescence in the upper and middle regions of the bed. At the same time, the use of high static bed conditions without destroying the stability of the device can increase the residence time of gas and coal particles, which is conducive to the exchange of heat and mass between the gas and solid phases, thus obtaining a higher syngas yield and fuel utilization efficiency.

Acknowledgement

The authors wish to acknowledge financial support by the Shandong Provincial Natural Science Foundation (ZR2020MB144), the Natural Science Foundation Project of Ningxia (2022AAC01001), the Key Research and Development Program of Ningxia (2022BSB03054), and the Joint Funds of the National Natural Science Foundation of China (U20A20124).

Conflict of interest

Authors declare no conflict of interest.

References

- [1] Wang, X.; Wang, X.; Kong, Z.; Shao, Y.; Jin, B. Auto-thermal operation and optimization of coal-fueled separated gasification chemical looping combustion in a pilot-scale unit. *Chem. Eng. J.* **2020**, *383*, 123159.
- [2] Zhang, Z.; Liu, Y.; Dai, Y.; Zhang, H.; Chen, Z.; Shen, Y.; Zhu, Z.; Wang, Y. Life Cycle environmental implications of Ionic-Liquid-Based carbon capture and storage processes and its alternative improvement cases. *ACS Sustain. Chem. Eng.* **2020**, *8*, 18106-18113.
- [3] Wang, Y.; Liu, X.; Zhang, H.; Liu, Y.; Cui, P.; Zhu, Z.; Ma, Y.; Gao, J. Comprehensive 3E analysis and multi-objective optimization of a novel process for CO₂ capture and separation process from syngas. *J. Clean. Prod.* **2020**, *274*, 122871.
- [4] Sultan, H.; Muhammad, H. A.; Bhatti, U. H.; Min, G. H.; Baek, I. H.; Baik, Y.-J.; Nam, S. C. Reducing the efficiency penalty of carbon dioxide capture and compression process in a natural gas combined cycle power plant by process modification and liquefied natural gas cold energy integration. *Energy Convers. Manag.* **2021**, *244*, 114495.
- [5] Mendiara, T.; Pérez-Astray, A.; Izquierdo, M. T.; Abad, A.; de Diego, L. F.; García-Labiano, F.; Gayán, P.; Adánez, J. Chemical looping combustion of different types of biomass in a 0.5 kW_{th} unit. *Fuel.* **2018**, *211*, 868-875.
- [6] Luo, M.; Yi, Y.; Wang, S.; Wang, Z.; Du, M.; Pan, J.; Wang, Q. Review of hydrogen production using chemical-looping technology. *Renew. Sustain. Energy Rev.* **2018**, *81*, 3186-3214.
- [7] Hu, Q.; Shen, Y.; Chew, J. W.; Ge, T.; Wang, C.-H. Chemical looping gasification of biomass with Fe₂O₃/CaO as the oxygen carrier for hydrogen-enriched syngas production. *Chem. Eng. J.* **2020**, *379*, 122346.
- [8] An, M.; Guo, Q.; Ma, J.; Hu, X. Chemical-looping gasification of coal with CuFe₂O₄ oxygen carriers: The reaction characteristics and structural evolution. *Can. J. Chem. Eng.* **2020**, *98*, 1512-1524.
- [9] Hu, J.; Li, C.; Zhang, Q.; Guo, Q.; Zhao, S.; Wang, W.; Lee, D.-J.; Yang, Y. Using chemical looping gasification with Fe₂O₃/Al₂O₃ oxygen carrier to produce syngas (H₂+CO) from rice straw. *Int. J. Hydrogen Energy.* **2019**, *44*, 3382-3386.
- [10] Adnan, M. A.; Hossain, M. M. Integrated drying and gasification of wet microalgae biomass to produce H₂ rich syngas - A thermodynamic approach by considering in-situ energy supply. *Int. J. Hydrogen Energy.* **2019**, *44*, 10361-10373.
- [11] Li, G.; Chang, Y.; Chen, L.; Liu, F.; Ma, S.; Wang, F.; Zhang, Y. Process design and economic assessment of butanol production from lignocellulosic biomass via chemical looping gasification. *Bioresour Technol.* **2020**, *316*, 123906.
- [12] Zhu, L.; Li, L.; Zhang, Z.; Chen, H.; Zhang, L.; Wang, F. Thermodynamics of hydrogen production based on coal gasification integrated with a dual chemical looping process. *Chem. Eng. Technol.* **2016**, *39*, 1912-1920.
- [13] Chen, C.; Werther, J.; Heinrich, S.; Qi, H.-Y.; Hartge, E.-U. CPFD simulation of circulating fluidized bed risers. *Powder Technol.* **2013**, *235*, 238-247.
- [14] Wang, Q.; Niemi, T.; Peltola, J.; Kallio, S.; Yang, H.; Lu, J.; Wei, L. Particle size distribution in CPFD modeling of gas-solid flows in a CFB riser. *Particuology.* **2015**, *21*, 107-117.
- [15] Bandara, J. C.; Jayarathna, C.; Thapa, R.; Nielsen, H. K.; Moldestad, B. M. E.; Eikeland, M. S. Loop seals in circulating fluidized beds - Review and parametric studies using CPFD simulation. *Chem. Eng. Sci.* **2020**, *227*, 115917.
- [16] Sung, W. C.; Kim, J. Y.; Chung, S. W.; Lee, D. H. Effect of particle size distribution on hydrodynamics of pneumatic conveying system based on CPFD simulation. *Adv. Powder Technol.* **2021**, *32*, 2336-2344.
- [17] Kraft, S.; Kirmbauer, F.; Hofbauer, H. Influence of drag laws on pressure and bed material recirculation rate in a cold flow model of an 8 MW dual fluidized bed system by means of CPFD. *Particuology.* **2018**, *36*, 70-81.
- [18] Lu, H.; Guo, X.; Jin, Y.; Gong, X.; Zhao, W.; Barletta, D.; Poletto, M. Powder discharge from a hopper-standpipe system modelled with CPFD. *Adv. Powder Technol.* **2017**, *28*, 481-490.
- [19] Wang, J. Continuum theory for dense gas-solid flow: A state-of-the-art review. *Chem. Eng. Sci.* **2020**, *215*, 115428.
- [20] Wang, S.; Luo, K.; Fan, J. CFD-DEM coupled with thermochemical sub-models for biomass gasification: Validation and sensitivity analysis. *Chem. Eng. Sci.* **2020**, *217*, 115550.

- [21] Kong, D.; Zhou, M.; Wang, S.; Luo, K.; Li, D.; Fan, J. Eulerian-Lagrangian simulation of chemical looping combustion with wide particle size distributions. *Chem. Eng. Sci.* **2021**, *245*, 116849.
- [22] Guo, X.; Chang, G.; Tan, X.; Hu, X.; Guo, Q. Experimental and numerical research on chemical looping gasification of coal char in a pressured fluidized bed reactor. *Acta Petrol. Sin.: Pet. Process. Section.* **2020**, *36*, 1294-1304.
- [23] Li, Z.; Xu, H.; Yang, W.; Wu, S. Numerical study on the effective utilization of high sulfur petroleum coke for syngas production via chemical looping gasification. *Energy.* **2021**, *235*, 121395.
- [24] Li, Z.; Xu, H.; Yang, W.; Zhou, A.; Xu, M. CFD simulation of a fluidized bed reactor for biomass chemical looping gasification with continuous feedstock. *Energy Convers. Manag.* **2019**, *201*, 112143.
- [25] Yang, J.; Hou, Z.; Chen, Z.; Ma, Z.; Li, S.; Wang, Y.; Gao, J.; Cui, P. Comprehensive analysis of diverse biochemical treatment technologies of fixed-bed coal gasification wastewater from the perspective of different weight dimensions. *Sep. Purif. Technol.* **2021**, *257*, 117889.
- [26] Zhao, H.; Tian, X.; Ma, J.; Chen, X.; Su, M.; Zheng, C.; Wang, Y. Chemical looping combustion of coal in china: comprehensive progress, remaining challenges, and potential opportunities. *Energy Fuels.* **2020**, *34*, 6696-6734.
- [27] Yu, Z.; Yang, Y.; Yang, S.; Zhang, Q.; Zhao, J.; Fang, Y.; Hao, X.; Guan, G. Iron-based oxygen carriers in chemical looping conversions: A review. *Carbon Resour. Convers.* **2019**, *2*, 23-34.
- [28] Ren, T.; Hu, X.; An, M.; Ma, J.; Guo, Q. Simulaiton of 1 MW_{th} coal chemical looping gasification process. *Acta Petrol. Sin.: Pet. Process. Section.* **2020**, *36*, 1253-1261.
- [29] Tu, Q.; Wang, H.; Ocone, R. Application of three-dimensional full-loop CFD simulation in circulating fluidized bed combustion reactors - A review. *Powder Technol.* **2022**, *399*, 117181.
- [30] Snider, D. M. Three fundamental granular flow experiments and CPFD predictions. *Powder Technol.* **2007**, *176*, 36-46.
- [31] Mahalatkar, K.; Kuhlman, J.; Huckaby, E. D.; O'Brien, T. Computational fluid dynamic simulations of chemical looping fuel reactors utilizing gaseous fuels. *Chem. Eng. Sci.* **2011**, *66*, 469-479.
- [32] Nakhaei, M.; Wu, H.; Grévaïn, D.; Jensen, L. S.; Glarborg, P.; Dam-Johansen, K. CPFD simulation of petcoke and SRF co-firing in a full-scale cement calciner. *Fuel Process. Technol.* **2019**, *196*,
- [33] Wu, Y.; Shi, X.; Liu, Y.; Wang, C.; Gao, J.; Lan, X. 3D CPFD simulation of gas-solids flow in the high-density downer with FCC particles. *Powder Technol.* **2020**, *373*, 384-396.
- [34] Zhang, Y.; Liang, Y.; Wang, M.; Bi, X.; Lu, C. Experimental study and CPFD simulation on circumferential flow heterogeneity in a disc-donut catalyst stripper. *Chem. Eng. J.* **2020**, *391*, 123567.
- [35] Steinke, C.; Kaliske, M. A phase-field crack model based on directional stress decomposition. *Comput. Mech.* **2018**, *63*, 1019-1046.
- [36] Luo, C.; Chen, L.; Huang, Y. A phase-field crack model based on a directional strain decomposition and a stress-driven Crack-Opening Indicator. *Comput. Methods Appl. Mech. Eng.* **2021**, *384*, 113928.
- [37] Yang, Z.; Zhang, Y.; Zhang, H. CPFD simulation on effects of louver baffles in a two-dimensional fluidized bed of Geldart A particles. *Adv. Powder Technol.* **2019**, *30*, 2712-2725.
- [38] Wang, X.; Jin, B.; Zhang, Y.; Zhang, Y.; Liu, X. Three Dimensional modeling of a coal-fired chemical looping combustion process in the circulating fluidized bed fuel reactor. *Energy Fuels.* **2013**, *27*, 2173-2184.
- [39] Zhang, R.; Wang, Q. H.; Luo, Z. Y.; Fang, M. X.; Cen, K. F. Coal char gasification in the mixture of H₂O, CO₂, H₂, and CO under pressured conditions. *Energy Fuels.* **2014**, *28*, 832-839.
- [40] Zhang, R.; Wang, Q. H.; Luo, Z. Y.; Fang, M. X.; Cen, K. F. Competition and inhibition effects during coal char gasification in the mixture of H₂O and CO₂. *Energy Fuels.* **2013**, *27*, 5107-5115.
- [41] Dymala, T.; Wang, S.; Jarolin, K.; Song, T.; Shen, L.; Dosta, M.; Heinrich, S. MP-PIC simulation of biomass steam gasification using ilmenite as an oxygen carrier. *Atmosphere.* **2022**, *13*, 1009.
- [42] Toshniwal, P.; Srivastava, V. Existence of synergistic effects during co-pyrolysis of petroleum coke and wood pellet. *Int. J. Chem. React. Eng.* **2017**, *15*, 20160046.
- [43] Chen, X.; Ma, J.; Tian, X.; Wan, J.; Zhao, H. CPFD simulation and optimization of a 50 kW_{th} dual circulating fluidized bed reactor for chemical looping combustion of coal. *Int. J. Greenh. Gas Control.* **2019**, *90*, 102800.
- [44] Jiang, H.; Chen, H.; Gao, J.; Lu, J.; Wang, Y.; Wang, C. Characterization of gas-solid fluidization in fluidized beds with different particle size distributions by analyzing pressure fluctuations in wind caps. *Chem. Eng. J.* **2018**, *352*, 923-939.
- [45] Li, C.; Wang, W.; Guo, X.; Duan, J. Fluidization characteristics of wide-size-distribution particles in a gas-solid fluidized bed reactor. *Int. J. Chem. React. Eng.* **2020**, *18*, 20200100.
- [46] Pedersen, S.; Durdevic, P.; Yang, Z. Challenges in slug modeling and control for offshore oil and gas productions:

A review study. *Int. J. Multiph. Flow.* **2017**, *88*, 270-284.

- [47] Pan, X.; Ma, J.; Hu, X.; Guo, Q. Energy and economic analysis of a hydrogen and ammonia co-generation system based on double chemical looping. *Chin. J. Chem. Eng.* **2021**, *36*, 190-198.
- [48] Yuan, P.; Guo, T.; Pan, X.; Hu, X.; Ma, J.; Xu, D.; Zhou, Z.; Guo, Q.; Guo, X. Process optimization and thermodynamic analysis of autothermal coal chemical looping gasification industrial demonstration system. *Fuel.* **2023**, *334*, 126667.